

Automated Defect Detection for Mass-Produced Electronic Components Based on YOLO Object Detection Models

Wei-Lung Mao, Chun-Chi Wang, Po-Heng Chou, *Member, IEEE*, and Yen-Ting Liu

Abstract—Since the defect detection of conventional industry components is time-consuming and labor-intensive, it leads to a significant burden on quality inspection personnel and makes it difficult to manage product quality. In this paper, we propose an automated defect detection system for the dual in-line package (DIP) that is widely used in industry, using digital camera optics and a deep learning (DL)-based model. The two most common defect categories of DIP are examined: (1) surface defects, and (2) pin-leg defects. However, the lack of defective component images leads to a challenge for detection tasks. To solve this problem, the ConSinGAN is used to generate a suitable-sized dataset for training and testing. Four varieties of the YOLO model are investigated (v3, v4, v7, and v9), both in isolation and with the ConSinGAN augmentation. The proposed YOLOv7 with ConSinGAN is superior to the other YOLO versions in accuracy of 95.50%, detection time of 285 ms, and is far superior to threshold-based approaches. In addition, the supervisory control and data acquisition (SCADA) system is developed, and the associated sensor architecture is described. The proposed automated defect detection can be easily established with numerous types of defects or insufficient defect data.

Index Terms—Deep learning (DL), You Only Look Once (YOLO), automated defect detection, camera sensor, automated optical inspection (AOI), dual inline package (DIP) switch, ConSinGAN.

I. INTRODUCTION

GLOBAL market trend [1] shows that the global market size of the dual in-line package (DIP) [2] switch achieved USD 400.1 million in 2021. Based on a compound annual growth rate of 3.3% during the forecast period, it is predicted to reach USD 554.35 million by 2031. It exhibits a steady annual growth with approximately 10 million units produced daily. With this huge amount of the manufacturing process, it is an essential issue to manage product quality and yield rates. However, conventional quality management

Manuscript received September xx; revised xx; accepted xx. Date of publication xx; date of current version xx. This work was supported in part by the National Science and Technology Council (NSTC) of Taiwan under Grant 112-2221-E-001-020-MY3, and in part by Academia Sinica under Grant 235g Postdoctoral Scholar Program (*Corresponding author: Chun-Chi Wang*).

Wei-Lung Mao and Chun-Chi Wang are with the Department of Electrical Engineering and Graduate School of Engineering Science and Technology, National Yunlin University of Science and Technology, Yunlin, 64002, Taiwan (e-mail: wlmao@yuntech.edu.tw, d11010202@gmail.yuntech.edu.tw).

Po-Heng Chou is with the Research Center for Information Technology Innovation (CITI), Academia Sinica, Taipei, 11529, Taiwan (e-mail: d00942015@ntu.edu.tw).

Yen-Ting Liu is with the Institute of Communications Engineering (ICE), National Sun Yat-sen University (NSYSU), Kaohsiung, 80424, Taiwan (e-mail: m113070007@student.nsysu.edu.tw).

depends on human visual product inspections. Due to the time-consuming and labor-intensive nature of the task, it leads to a significant burden on quality inspection personnel. Therefore, the current trend of Industry 4.0 is to streamline manufacturing industries, converting from labor-intensive work toward deep learning (DL)-based automated production.

Over the past decade, DL [3]–[6] has been widely applied to various fields, including image recognition, natural language processing, autonomous driving, and object classification problems. Further, DL has also been used for medical radiography image detection and classification [7]–[10], A. Jo and W. Lee, [11] proposed a method of deep learning models for material discrimination and quantitation. S. M. J. Jalali *et al.*, [12] proposed a method of deep reinforcement learning-based ensemble algorithm that integrates optimized deep learning models to minimize wind power forecasting errors for two wind power datasets. In [13], a method of deep learning was proposed by E. Jeong *et al.* for heterogeneous inference parallelization.

Several works [14]–[16] use DL to reduce labor resource consumption and promote production line automation. In [14], a dual-weighted analysis algorithm was proposed by K. Qiu *et al.* for metal defect detection. Y. Chen *et al.* [15] focused on improving the metal punching position using fiber Bragg grating (FBG) sensors and identifying the impact source location through a hyperbolic localization model. In [16], A. Albanese *et al.* developed a system using a micro-camera control unit (MCU) for automatic DL imaging and detection. Several studies [17]–[20] use DL and threshold-based methods to detect defects. L. Xiao *et al.* [17] utilized wavelet transformations to process image features for surface defect detection. Y. Zhang *et al.* [18] formulated defect detection as a classified problem, which could then be resolved via support vector machines (SVM) and random forests (RF). S. Tian *et al.* [19] proposed a complementary adversarial network-driven surface defect detection (CASDD) framework to identify different types of texture defects automatically and accurately. Y. Peng *et al.* [20] proposed a method to detect surface defects on electric distribution cabinets using SVM and Gaussian distribution modeling threshold techniques. A. Dairi *et al.* [21] proposed a novel stereo-vision method that merges a deep encoder with k nearest neighbor (KNN) for anomaly detection to detect obstacles in a road environment. In [22], A. Dairi *et al.* proposed a deep encoder with a one-class support vector machine (OCSVM) for obstacle detection systems. Table I summarizes the applications and objects of

the methods above.

TABLE I: Comparison of defect detection methods

Methods	Model / Algorithm	Detected objective	Goal
DL	CNN	Test components [16]	Surface defect
		Test components [15]	Object positioning
		Steel [19]	Surface defect
	IPCNN	Car [17]	Oil leak detection
Threshold	KNN	Obstacle [21], [22]	Obstacle detection
	OCSVM		
	Wavelet multiscale analysis	Tire [18]	Surface defect
Gaussian distribution modeling, SVM	Electric distribution cabinet [20]		Surface defect
	Dual-weighted analysis algorithm	Metal parts [14]	Surface defect

However, these studies overlooked several key aspects: 1) Real-time detection: Most studies focus on performance in terms of accuracy, and neglect the detection speed performance in the practical application. 2) Computational limitations: It is crucial to lighten the DL model to fit hardware constraints, rather than increasing its size indefinitely for computational capability. 3) Insufficient dataset: The lack of datasets leads to a challenge for detection tasks.

Therefore, we design the lightweight DL model to fit hardware limitations and real-time detection capability. From the review of the image detection models [23]–[26], we selected anchor-based one-stage models, specifically the You Only Look Once (YOLO) [27]–[33].

YOLO is a neural network that has shown superior performance in terms of both real-time operation and accuracy. YOLO uses the feature pyramid network (FPN) framework enhancement for iterative updates to achieve better results until convergence. YOLO has demonstrated commendable performance in various high-demand real-time scenarios such as public face recognition, mask detection, self-driving car systems, automated manufacturing systems, surface defect detection, etc. Several studies [34]–[46] suggested using YOLO for the dynamic detection of metal surface defects [34], [35], [37], [38]. The authors of [36] applied YOLO to real-time detection for traffic signs. The authors of [43] performed a visual detection of autonomous robots by YOLO. Furthermore, improved YOLO models were used to detect surface defects in solar cells in [40] and [44]. YOLO has also been used for real-time detection of ships [39], [41] and vehicles [42], [45], [46].

To the best of our knowledge, this work is the first study to investigate DL-based automated DIP image detection. A quality-control defect detection method is proposed for each side of this hexagonal component. The proposed system is not a stand-alone system but is integrated with automated manufacturing production line processes. Therefore, the detection time of the automated production output from the preceding workstation must be considered to ensure that detection is completed within a specified time frame.

On the other hand, the primary challenge of automated image processing is the scarcity of defective product samples. To enhance the limited amount of samples, a generative adversarial network (GAN) model [47] called ConSinGAN [48] is used to increase the input image quantity for data augmentation. The ConSinGAN can develop a model based on a single

image and effectively simulate the defect characteristics in the generated image. It greatly facilitates the training process of detection models. The other GANs, such as deep convolutional GAN (DCGAN) [49] or Wasserstein GAN (WGAN) [50], require more images for training. The main contributions of this paper are described as follows:

- The proposed defective DIP detection system is designed based on the YOLO model to improve the quality of the inspection.
- To enhance the performance of the YOLO model, ConSinGAN is used to generate the amount of DIP image data for the training phase.
- To validate the effectiveness, we develop a practical production line and SCADA interface to reflect the performance in practical applications.
- To compare the different YOLO versions, we evaluate the performances in terms of accuracy and detection time.
- Compared with threshold-based detection, the proposed YOLO models with ConSinGAN reveal a reduction in production detection time by 909–948 ms, where the YOLOv7 with ConSinGAN achieves an accuracy of 95.50%.
- Unlike previous studies that only focused on detection models, we implement the proposed detection in a practical automated mechanism, while considering the detection time for performance measurement.

The remainder of this paper is organized as follows. Sec. II presents the architecture of the automated defect detection system, the types of DIP defects, and threshold-based image detection for baseline comparison. Sec. III details the data pre-processing, YOLO models, and performance metrics. Sec. IV compares the simulation results among the threshold-based detection, DL-based YOLOv3, v4, v7, and v9 models with/without ConSinGAN for DIP defect detection. Sec. V summarizes the conclusions and the future works.

II. AUTOMATED DEFECT DETECTION SYSTEM

The system architecture is shown in Fig. 1 and includes three parts: 1) Control system: Comprised of a personal computer (PC) and the programmable logic controller (PLC) devices. The PC is used to interact with the imaging equipment and establish the SCADA, which allows for integration with the DL model and data analysis. The PLCs are used to connect the mechanical equipment, control various actions, issue action completion signals, and provide a secondary confirmation count. 2) Imaging equipment: industrial cameras, centrifugal lenses, and various light source equipment. The imaging equipment interacts and feeds data to the PC via an Ethernet cable (RJ45). 3) Mechanical equipment: The human-machine interface of the PLC includes pneumatic clamps, electromagnetic push rods, and solenoid valves.

A. Automated Mechanism

The proposed system is designed to inspect all six sides of the workpiece. Each side is equipped with multiple Automated Optical Inspections (AOI) at different locations to minimize interference from various light sources on different surfaces.

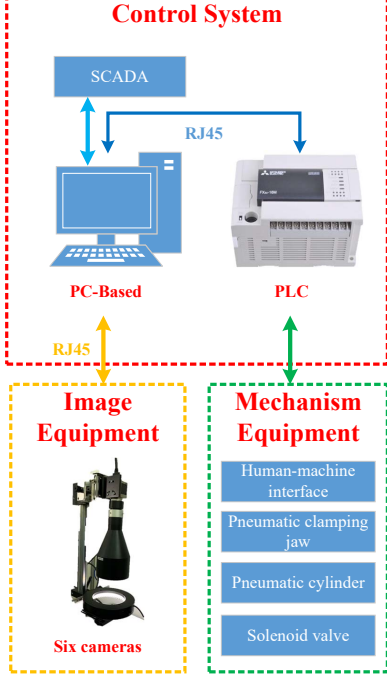


Fig. 1: System architecture diagram.

A 3D schematic diagram of the proposed system architecture is shown in Figure 2. Fig. 2 shows the position and orientation of the AOI and the design of the experimental fixture. It establishes the positioning of lenses and light sources at different angles to inspect the long and short sides of a rectangular workpiece. The detected DIP is placed inversely at the production line. Thus, the DIP top-side detection uses the camera to capture images from bottom to top, and the DIP bottom-side detection captures images from top to bottom. The back- and front- sides of DIP are shot using two sets of cameras from the left and right. Side-to-side imaging is facilitated by rotating the device, allowing cameras on both sides to capture images. The longer sides are the up, down, back, and front parts of the detected DIP. The shorter sides are the left and right of the detected DIP. To examine the longer and shorter surfaces of rectangular DIP, the experiment required two sets of cameras and lenses, each with a specific depth of field. Long-side cameras use a low depth of field, and short-side cameras use a high depth of field. Tables II and III list the specific parameters of the camera lens set.

TABLE II: Low depth of field camera and lens specifications

BASLER-acA4096-30 μm (Camera)		SPO-2001-4M (Len)	
Specification	Parameter	Specification	Parameter
Pixel size	3.45 μm	Depth of field	4.5
Image resolution	4096 \times 2168	Working distance	200
Magnification	0.231	Field of view (FOV)	61.0 \times 33.4

TABLE III: High depth of field camera and lens specifications

BASLER-acA3800-14 μm (Camera)		OPTO-TC23048(Len)	
Specification	Parameter	Specification	Parameter
Pixel size	1.67 μm	Depth of field	20.0 mm
Image resolution	3860 \times 2748	Working distance	132.9 mm
Magnification	0.184	Field of view (FOV)	34.9 \times 24.9 mm

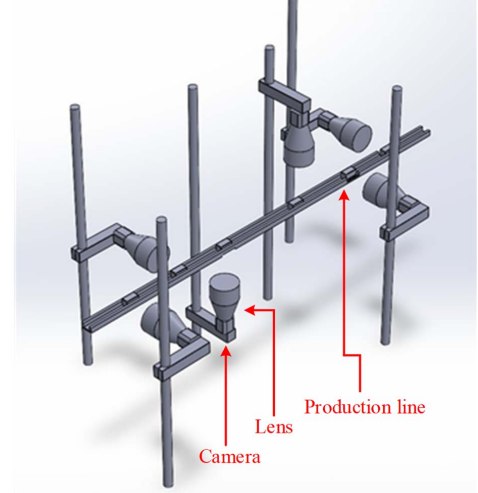


Fig. 2: 3D simulation schematic.

The size of each workpiece is approximately 21.7 mm $\text{pm}0.5$ mm on the long side and 9.4 mm $\text{pm}0.4$ mm on the short side. The resolving power of the image equipment is calculated by

$$RP = \frac{PS}{MF}, \quad (1)$$

where RP is the resolving power, PS is the pixel size, and MF is the magnification. The field of view (FOV) is calculated by

$$\text{FOV} = RP \times IR, \quad (2)$$

where IR is the image resolution.

B. Types of Defective DIP

A normal DIP switch is shown in Fig. 3. For defective DIPs, there are two categories: surface and pin-leg. The surface defects include three types: surface overflow, surface scratches, and surface contamination. In addition, misaligned pin-legs are also a type of defect. The above four defective DIPs are shown in Fig. 4.

The sizes of the defect feature are as follows: Fig. 4(a) is approximately 100 to 300 pixels, Fig. 4(b) is approximately 100 to 500 pixels, Fig. 4(c) is approximately 100 to 300 pixels, and Fig. 4(d) is 220 to 250 pixels per pin. To enhance the contrast degree of the feature, the images in Fig. 4(a), 4(b), 4(c), and 4(d) can use the red green blue (RGB) channel subtraction, such as red (R) minus green (G) and G minus blue (B) to enhance the features of the image.

C. Threshold-Based Image Detection

For a baseline comparison, we introduce a threshold-based image detection. First, it performs binary classification of the original image using a preset threshold to obtain the featured image. The feature extraction is determined by

$$b(x, y) = \begin{cases} 255, & \text{MinGray} \leq g(x, y) \leq \text{MaxGray}, \\ 0, & \text{otherwise,} \end{cases} \quad (3)$$

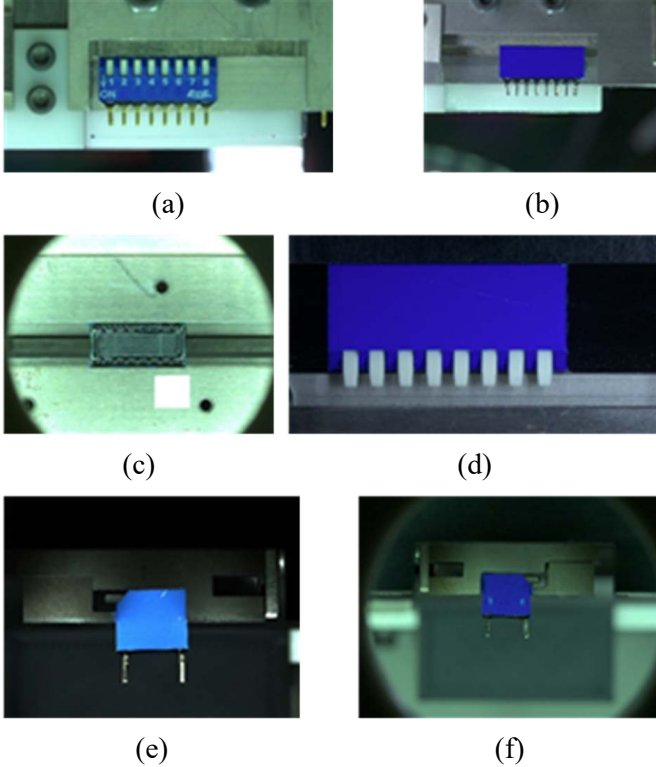


Fig. 3: Different sides of Normal DIP, (a) front, (b) back, (c) bottom, (d) top, (e) right, and (f) left sides.

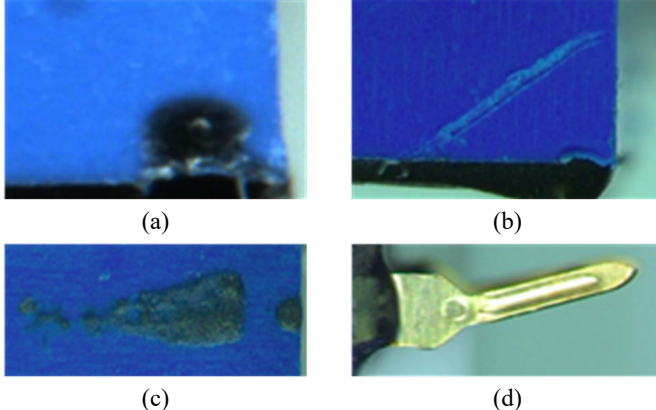


Fig. 4: Four types of defective DIP, (a) surface glue overflow, (b) surface scratches, (c) surface dirt, and (d) bent pins.

where $b(x, y)$ represents the pixel of the featured image based on the binary decisions, $g(x, y)$ is the pixel of the original image, MinGray is the minimum threshold, and MaxGray is the maximum threshold.

Since the light intensity corresponding to each camera varies with the six sides of the DIP surface, the threshold values MinGray and MaxGray are adjustable. Whether each side of the DIP surface is defective or not is determined by

$$DR(z) = \begin{cases} \text{defective DIP, } TB \leq o(z) \\ \text{Normal DIP, } TB > o(z) > 0, \end{cases} \quad (4)$$

where $DR(z)$ represents the threshold-based detected result, TB represents the preset threshold, z denotes the featured image, and $o(\cdot)$ is the output image of feature extraction. The features of defective DIP are shown in Fig. 5.

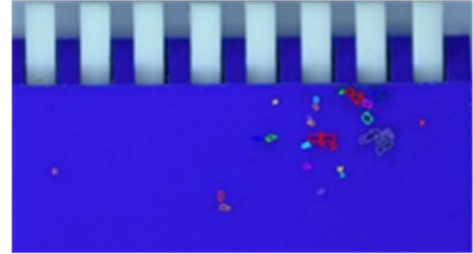


Fig. 5: The defective features from threshold-based detection.

III. DL-BASED YOLO MODEL AND CONsingAN

Fig. 6 shows the workflow of the proposed detection. To select the outstanding YOLO version, we compare different YOLO versions in terms of accuracy, floating-point operations (FLOPs), and the number of parameters. To enhance the accuracy of the YOLO models, we augment the data set by using ConSinGAN [48] during the data pre-processing. The ConSinGAN modifies the original images using rotation, translation, flipping, scaling, Gaussian noise, etc, for data augmentation.

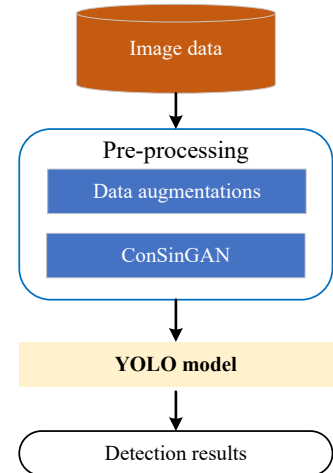


Fig. 6: The flow chart of the proposed defective DIP detection.

A. Data Pre-Processing

1) *Data Augmentation*: To augment the defective DIP image dataset, various techniques are used: flipping, mirroring, brightness adjustment, median filtering, noise, and Gaussian blur, as depicted in Fig. 7. Data augmentation is crucial to improve the trained model and enhance the discrimination.

2) *ConSinGAN*: The predecessor of ConSinGAN, SinGAN [51], introduces a GAN that is trained on a single image for tasks such as unconditional image generation and harmonization. The Concept of the ConSinGAN model is shown in Fig. 8.

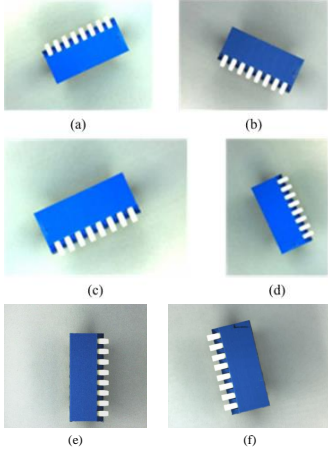


Fig. 7: Image augmentation. (a) brightness adjustment, (b) mirroring, (c) median filtering, (d) flipping, (e) noise, and (f) Gaussian blur.

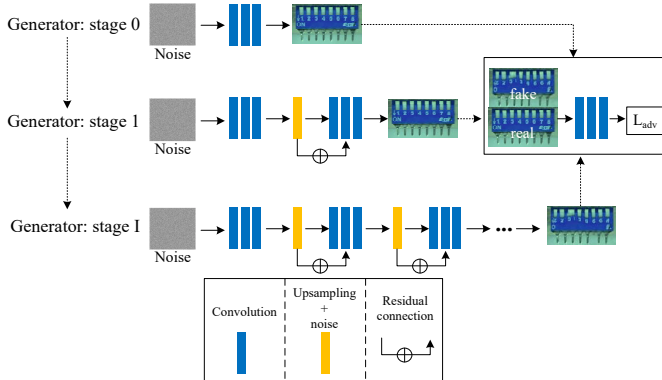


Fig. 8: The concept of the ConSinGAN.

ConSinGAN is trained using a multi-stage and multi-resolution approach with the lowest resolution (e.g., 25×25 pixels) in the first stage. The next stage increases the layers of the neural network and image resolution. At each stage, the layers of the neural network in all the previous stages are frozen, and only the current added layers of the neural network are trained. Different from the traditional GAN, it uses a multi-generator, and the number of stages increases the number of generators. The traditional GAN propagates feature maps from one generator stage to the next, which leads to a negative effect on learning performance. The training of ConSinGAN is limited to one stage at a specific time to prohibit interactions between different stages. If all stages are end-to-end training, it causes overfitting in the single-image case, and the network collapses. It means that the relationship between the receptive field and the size of the generated image decreases as the number of stages increases. At higher resolutions, the discriminator focuses on the texture of the image. At lower resolutions, the discriminator concerns the global layout of the image. At a given stage i , ConSinGAN optimizes the sum of an adversarial and a reconstruction loss, and initializes the discriminator with the weights of the

previous stage $i - 1$ at all stages as follows:

$$\min_{G_i} \max_{D_i} \mathcal{L}_{adv}(G_i, D_i) = \alpha \mathcal{L}_{rec}(G_i), \quad (5)$$

where $\mathcal{L}_{adv}(G_i, D_i)$ is the adversarial loss that is the same with WGAN [50], the reconstruction loss $\mathcal{L}_{rec}(G_i)$ is used to improve the training stability (α is set to 10 in our experiments) as follows:

$$\mathcal{L}_{rec}(G_i) = \|G_i(s_0) - s_i\|_2^2. \quad (6)$$

At the given resolution of stage i , we input (s_0) into the generator $G_i(s_0)$. The input (s_0) is a downsampling version of the original image (s_i) .

B. YOLO Learning Series

YOLO is adopted as a DL-based object detection algorithm. Compared with traditional object detection algorithms, the YOLO model can quickly perform object detection and classification within a single neural network. The YOLO architecture is a convolutional neural network (CNN) that includes multiple convolutional and fully connected layers, segments an image into $S \times S$ grids, and then detects multiple objects in each grid. In addition, the selection criteria of the different YOLO versions for DIP testing were based on their floating-point operations (FLOPs) and mAP. To compare different YOLO versions, we list the performance in terms of FLOPs, and of YOLO v3, v4, v5, v6, v7, v8, and v9, as shown in Table IV. YOLOv7 [29] is chosen as the proposed DIP testing model. In our simulation, YOLOv3 [27], YOLOv4 [28], and the current newest YOLOv9 [33] are considered for comparison. As shown in Table VI, the YOLOv7 slightly outperforms YOLOv9 in terms of accuracy but is slightly slower. YOLOv5 [30] and YOLOv6 [31] have similar FLOP performance to YOLOv7, but their mAP is less than that of YOLOv7. YOLOv8 has higher computation complexity than YOLOv7 in terms of FLOP by 63%; however, the mAP improved by only 0.1%. Therefore, YOLOv5, v6, and v8 are excluded from our main simulations.

TABLE IV: Comparison of the YOLO series

Model	#Param (M)	FLOPs	mAP0.5
YOLOv3 [27]	62	1457B	57.9%
YOLOv4 [28]	53	109B	65.7%
YOLOv5-L [30]	46.5	109.1G	67.3%
YOLOv6-M [31]	34.9	85.8G	66.4%
YOLOv7 [29]	36.9	104.7G	69.7%
YOLOv8-L [32]	43.7	165.2G	69.8%
YOLOv9-C [33]	25.3	102.1G	70.2%

To further compare the YOLOv3, v4, v7, and v9 models, we introduce the upgraded parts of these models in the following:

1) *YOLOv3* [27]: The most significant improvement of YOLOv3 is adopting the multiscale feature extraction, also known as a feature pyramid network (FPN). In addition, YOLOv3 uses binary cross-entropy as the loss function, instead of the mean square error of YOLOv2 [53]. YOLOv3 uses darknet-53 to replace darknet-19 of YOLOv2 and increase depth and accuracy, but it sacrifices the detection speed.

2) *YOLOv4* [28]: First, YOLOv4 uses CSPDarknet53 to establish the primary backbone neural network, making it a lightweight model while maintaining high accuracy. Second, YOLOv4 adopts spatial pyramid pooling [54] and path aggregation network [55] in the neck section to combine feature maps at different scales and detect different sizes of objects. Finally, the YOLOv4 employs CIoU-loss to evaluate the distance between the targeted and the predicted boxes and improve the accuracy.

3) *YOLOv7* [29]: YOLOv7 [29] and YOLOv4 [28] were developed by H.-Y. M. Liao, *et al.* The backbone of YOLOv7 is redesigned based on v4. The backbone is used to extract the features from the input images. Unlike YOLOv5 and v6, YOLOv7 is not pre-trained on ImageNet. YOLOv7 has several new architectures with improved performances in terms of accuracy and detection speed. The architecture of YOLOv7 is shown in Fig. 9

In Fig. 9, YOLOv7 uses extended ELAN (E-ELAN), which develops the original ELAN architecture through expanding, shuffling, and merging. These approaches allow the network to learn more diverse features without disrupting the original gradient paths. The head part of YOLOv7, which is used for object detection and localization, continues to utilize the head network structure of YOLOR [56]. The CBS block includes the convolutional layer, batch normalization, and the Silu activation function. The CBM block consists of the convolutional layer, batch normalization, and the Sigmoid activation function. REP block represents the RepVGG. The difference between MP-1 and MP-2 is the output size within the block. The difference between E-ELAN and ELAN-W is the output size within the block. The main improvements of YOLOv7 are as follows:

- In RepConv, the identity connection (id) disrupts the residual in ResNet and the concatenation in DenseNet. However, RepConv needs to retain features that provide greater gradient diversity for different feature maps. A novel weight parameterization approach is proposed in [57] for RepConv to replace id. In Fig. 10, the planned reparametrized convolution designed for ResNet is called RepConvN [29]. Since PlainNet in Fig. 10(a) inherently lacks residual or concatenation characteristics, RepConv in Fig. 10(b) can be applied directly. Since ResNet in Fig. 10(c) inherently has residual characteristics, RepConv in Fig. 10(d) leads to a decrease in accuracy. Based on the above reasons, YOLOv7 uses RepConvN (RepConv without id) to design a network architecture.
- Supervised learning is commonly used to train deep networks, where the weights of shallower layers are trained using an auxiliary mechanism to improve the accuracy of YOLOv7. In addition, YOLOv7 introduces a novel dynamic label assignment strategy that employs a coarse-to-fine guide to enhance feature learning. The final output head is called the lead head, and the head used for auxiliary training is called the auxiliary head. Fig. 11 depicts an object detector equipped with an auxiliary head.

- By optimizing ELAN, as shown in Fig. 12(a), the shortest and longest gradient paths are controlled to allow deeper layers to learn and converge more effectively. However, stacking more CNN layers in ELAN may disrupt stable learning. Therefore, YOLOv7 proposes extended ELAN (E-ELAN) in Fig. 12(b) to maintain gradient paths while continuously enhancing the learning performance using expanding, shuffling, and merging of cardinalities.

4) *YOLOv9* [33]: YOLOv9 introduces two novel techniques, including programmable gradient information (PGI) and generalized efficient layer aggregation network (GELAN). The descriptions of PGI and GELAN are as follows:

- The PGI theory involves redesigning a technique called the auxiliary reversible branch that allows the YOLOv9 to generate reliable gradient information during the training phase and pass it to the main branch.
- GELAN combines the functions of CSPNet and ELAN networks. It splits the input of each computational unit into two parts: one part is directly passed to the output, while the other part is transformed by the computational unit. Then, these two parts of computation are combined to form the final output. Thus, GELAN integrates information between computational units while enhancing flexibility and generalization.

The proposed model consists of two parts: data augmentation with ConSinGAN and training the YOLO model. The limitations of the YOLO model are as follows:

- Computational capability: Depending on the constraints of hardware, it is necessary to use a lightweight YOLO model, which may sacrifice accuracy.
- Training cost: To achieve accurate detection, the YOLO model requires a large amount of labeled data for training because collecting and labeling sufficient training data is a time-consuming and costly task.
- External factors: In the image, additional obstacles or illumination changes may reduce the accuracy of the YOLO model.
- Size of defect features: If the defect features are tiny, the single-stage detection is inferior to multi-stage detection.

C. Performance Evaluation

The leave-one-out cross-validation (LOOCV) is used to measure the performance of the proposed DIP detection system. The testing set includes one subject's data, while the training set uses the remaining subjects' data. LOOCV is repeated k times, where k is the total number of subjects, until all subjects have been used as the testing set. By using k -folds, the average performance can be obtained.

In our experiments, we adopt a confusion matrix as performance measurement, and five evaluation metrics, precision (PRE), recall (REC), F1-Score ($F1$), false positive rate (FPR), and true negative rate (TNR) as shown from Eq. (7) to (11) to measure the detection performance.

$$PRE = \frac{TP}{TP + FP}, \quad (7)$$

$$REC = \frac{TP}{TP + FN}, \quad (8)$$

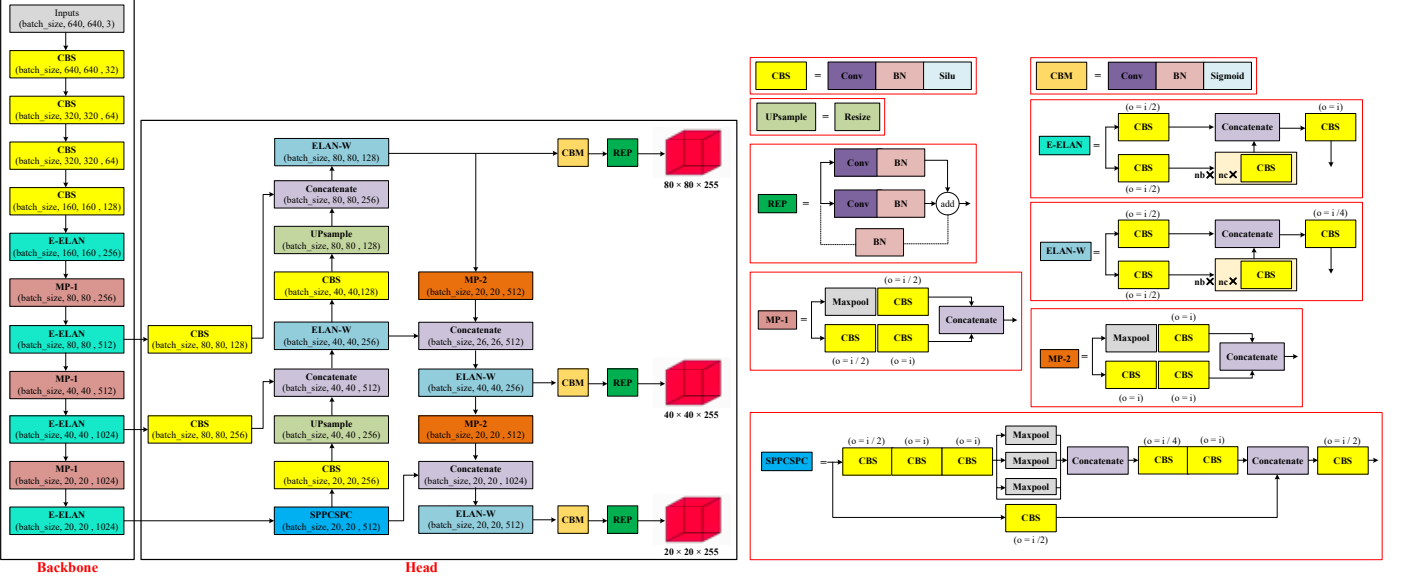


Fig. 9: The YOLOv7 network architecture and block description.

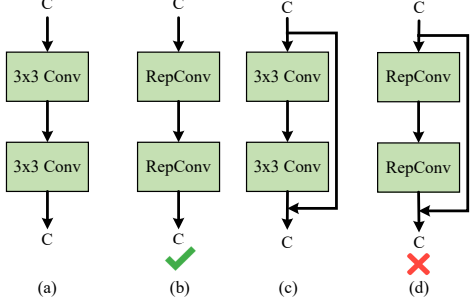


Fig. 10: The proposed RepConvN using (a) PlainNet, (b) RepPlainNet, (c) ResNet, and (d) RepResNet.

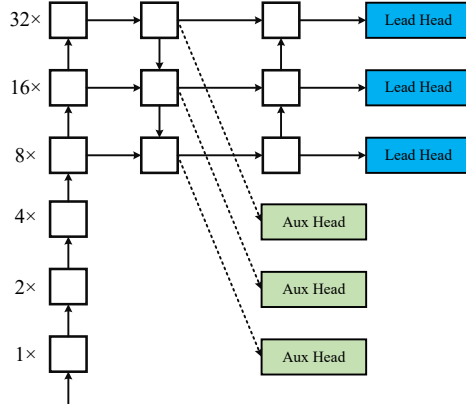


Fig. 11: YOLO model with auxiliary head.

$$F1 = 2 \times \frac{PRE \cdot REC}{PRE + REC}, \quad (9)$$

$$FPR = \frac{FP}{FP + TN}, \quad (10)$$

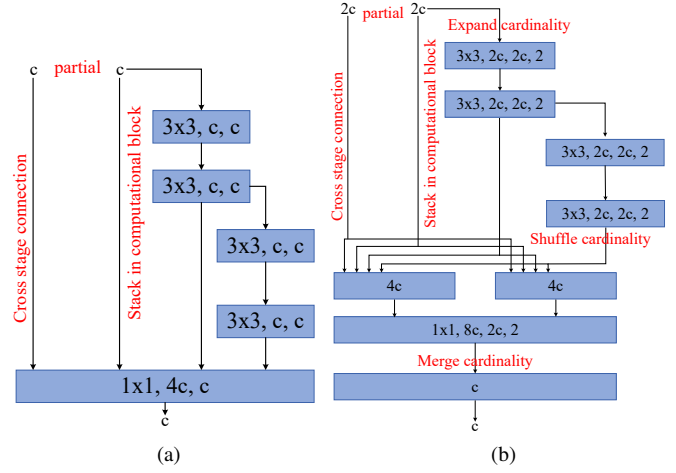


Fig. 12: ELAN optimization schematic for (a) ELAN, and (b) E-ELAN.

$$TNR = \frac{TN}{FP + TN}, \quad (11)$$

where TP (true positive), TN (true negative), FP (false positive), and FN (false negative) represent the cases: the defect and normal DIPs labeled as such are correctly recognized, the normal DIPs labeled as defective DIPs are misclassified, and the defective DIPs labeled as normal DIPs are misclassified, respectively.

The performance evaluation of detection depends on the intersection over the union (IoU), and mean average precision (mAP), where mAP0.5 means the threshold of YOLO is set to 0.5. All model training is conducted on a PC with an Intel 13th Gen I7-13700K CPU (3.40 GHz), Nvidia RTX4080 graphics card with 16 GB of dedicated memory, running on a 64-bit Windows 10 operating system. The training and testing phase for the models is executed in an Anaconda (a

Python derivative) environment, and the SCADA interface is integrated using Visual Studio 2019.

IV. EXPERIMENTAL RESULTS

In our experiments, the nine kinds of models are specified as follows: 1) Threshold-based detection, 2) YOLOv3, 3) YOLOv4, 4) YOLOv7, 5) YOLOv9, 6) YOLOv3 with ConSinGAN, 7) YOLOv4 with ConSinGAN, 8) YOLOv7 with ConSinGAN, 9) YOLOv9 with ConSinGAN. The hyperparameter settings of these models are as follows:

- The threshold-based detection: Based on Eq. (4), TB is assigned a constant value of 100.
- The proposed YOLOv3, v4, v7, and v9 models with/without ConSinGAN: Batches = 32, images = 416×416 , learning rate = 0.001, and maximum batches = 10000.

The hyperparameter settings for the generative adversarial network ConSinGAN are as follows: Learning rate = 0.1, the number of trained stages = 10, and the original images are captured using the industrial camera described in Sec. II. The total number of original images is 672. The ConSinGAN selects images with significant defective features for image augmentation. The total number of generated images is 3,183.

A. DIP images dataset

1) *ConSinGAN Augmentation*: Initially, GAN and DCGAN were used to augment data. However, the training performances of GAN and DCGAN were poor because of the limited number of defective image samples. Therefore, ConSinGAN is used, which generates similar images from a smaller number of images for data augmentation. The original images are shown in Fig. 13, and the augmented results are shown in Fig. 14. The amount of each side of the defective DIP in the generated dataset is shown in Table V.

TABLE V: Statistics of ConSinGAN-generated images.

Type of defect	Front	Back	Top	bottom	Left	Right	Total
Surface defect	340	228	209	183	310	346	1616
Pin defect	321	216	201	177	325	327	1567

B. Performances of YOLO with/without ConSinGAN

The YOLO model is trained for each aspect of the generated image data. These 3,183 images are divided into two categories: surface defects (surface overflow, surface scratches, and surface dirt) and pin defects (pin misalignment). We compare YOLOv3, v4, v7, and v9 with/without the ConSinGAN augmented sets to identify the optimal model. The training set is conducted on 80% of the dataset, i.e., 2,547 images. The validation set is adopted on the other 10% (318 images). The remaining 10% (318 images) are used for the testing set. Within this dataset, we define two distinct defect types that include: 1) Surface defects account for approximately 50.7% of defects, and 2) Misaligned pins account for 49.3%. Table VI demonstrates the performances of YOLOv3, v4, v7, and v9

with/without the ConSinGAN in terms of average precision (mAP) rate, *PRE*, *REC*, *F1*, *FPR*, and *TNR* evaluations of all six YOLO models.

As shown in Table VI, 1) With ConSinGAN, YOLOv3, v4, v7, and v9 outperform the models without ConSinGAN in terms of accuracy metrics due to data augmentation. By data augmentation, the YOLOv3, v4, v7, and v9 have been enhancing the performance in the training phase because of the increase in the amount of training data. 2) YOLOv7 with ConSinGAN achieves outstanding performance on accuracy metrics and outperforms the current newest YOLOv9 with ConSinGAN. The proposed YOLOv7 with ConSinGAN model achieves an accuracy in terms of $mAP0.5 = 95.5\%$ and outperforms the other models. However, the detection speed of YOLOv9 with ConSinGAN outperforms the other models and is slightly better than YOLOv7 with ConSinGAN. The detection time of each model is approximately 300 ms. Therefore, we select the YOLOv7 model in a DIP image detection system on the SCADA interface for the user, as illustrated in Fig. 15. In addition, ConSinGAN is only used to augment the dataset. Thus, it does not impact the complexity of YOLO models.

C. Performances of Threshold-based Detection

For baseline comparison, we introduce the performance evaluation of threshold-based detection. Table VII presents the number of images, accuracy, and detection time from different sides of DIP by threshold-based detection. Each workpiece is inspected from all six sides. The number of images is the same as in the YOLO experiments. The threshold value is set to 0.5. The accuracy is calculated by

$$A = \frac{DT - F}{DT} \times 100\%, \quad (12)$$

where A represents the accuracy, DT is the total number of detections, F is the number of detection errors.

Table VII shows the average accuracy is 87.81% on six-sided DIP image detection. The total detection time is 3.807 seconds, which matches the detection time. Our experiment involves an actual production line machine, divided into six-sided detectors that are moved synchronously. Therefore, the detection time is determined by the station with the longest detection time. The proposed YOLOv7 with ConSinGAN model outperforms the threshold-based system, achieving an accuracy of 95.5%.

D. Comparison of Detection Speed

Fig. 16 demonstrates the detection time of the YOLO models and shows a significantly higher detection speed than the threshold-based system. The threshold-based method needs to reset the parameters for every six-sided DIP image. However, YOLO models only need one setting, because the training and testing stages are both performed using six-sided DIP images as input. Different from threshold-based image processing, YOLO models do not require parameter adjustments to different sides of DIP to obtain accurate results. Thus, there are performance gaps between YOLO models and the threshold-based method. From Fig. 16, it is feasible to replace the

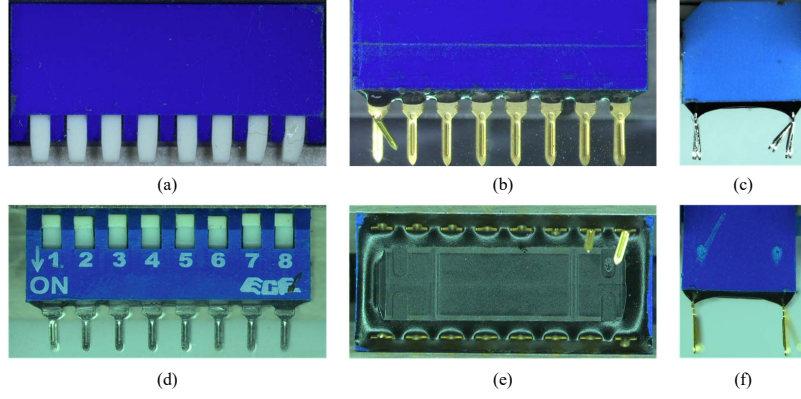


Fig. 13: Original images of defective DIP, (a) top, (b) back, (c) right, (d) front, (e) bottom, and (f) left sides.

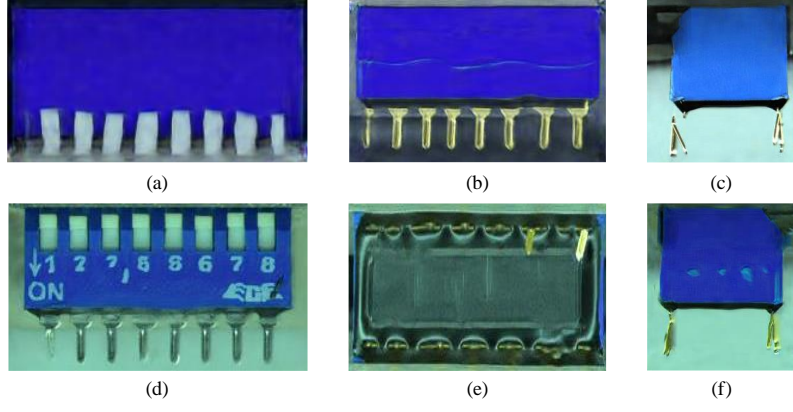


Fig. 14: Images generated by ConSinGAN, (a) top, (b) back, (c) right, (d) front, (e) bottom, and (f) left sides.

TABLE VI: Performance Comparison of YOLO models.

Model	mAP0.5	PRE	REC	F1	FPR	TNR	Detection time (ms)
YOLOv3	66.2%	73.2%	51.5%	61.8%	35.0%	64.9%	322
YOLOv4	65.4%	80.1%	61.4%	68.9%	35.2%	64.8%	314
YOLOv7	65.1%	84.2%	58.6%	68.1%	34.3%	65.6%	297
YOLOv9	74.5%	79.2%	66.4%	72.8%	40.3%	59.7%	279
YOLOv3 with ConSinGAN	91.9%	92.8%	91.4%	92.4%	8.9%	91.1%	321
YOLOv4 with ConSinGAN	89.1%	91.3%	92.6%	91.5%	10.7%	89.2%	310
YOLOv7 with ConSinGAN	95.5%	94.9%	90.7%	93.4%	3.7%	96.4%	285
YOLOv9 with ConSinGAN	90.5%	87.7%	82.9%	85.0%	9.8%	90.2%	278

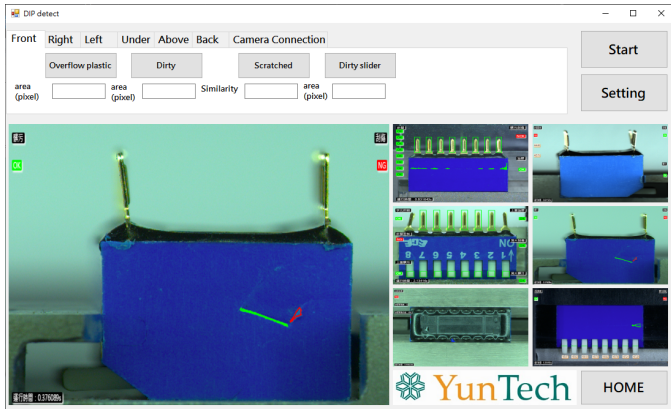


Fig. 15: The SCADA interface.

threshold-based image-processing defect detection rate with the proposed YOLOv7 with the ConSinGAN approach.

TABLE VII: Performance of the threshold-based detection

Detected side	Test number	Accuracy	Detection time (ms)
Left	635	86.30%	290
Top	410	86.58%	391
Right	673	88.85%	359
bottom	360	92.22%	815
Back	444	90.54%	721
Front	661	84.56%	1231
Total	3183	87.81%	3807

V. CONCLUSION

In this paper, our goal is to establish an AOI system for defective DIP detection to improve the quality of production and save human efforts. We use the SCADA interface to

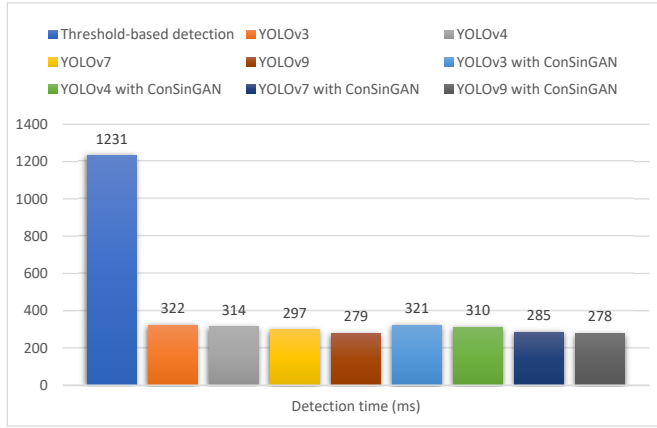


Fig. 16: Comparison of detection speed.

integrate image detection and automated mechanism hardware for a large number of DIP inspections. For the image detection model, we use threshold-based detection and DL-based YOLO models. The threshold-based detection outperforms the YOLO models in terms of accuracy. However, the threshold-based detection is time-consuming. Thus, we adopt ConSiGAN to augment the dataset for YOLO training and improve the accuracy. With ConSiGAN, YOLOv7 achieves an accuracy of 95.5%, outperforming the accuracy of 87.81% by threshold-based detection. The detection times of different YOLO models are 285 to 322 ms, which outperforms 1231 ms of the threshold-based detection. In summary, ConSiGAN effectively enhances the accuracy of YOLO models while maintaining the outstanding detection time. For future works, we summarize as follows:

- Applying future novel models to improve the detection model network.
- Increasing the variety of workpieces for the automated detection system, such as rotating DIP and surface mount devices, which are mass-produced electronic components.
- Expanding the SCADA system to cover additional production lines, aiming for smart factories and AIoT integration.

REFERENCES

- [1] Digit. Journal, “DIP switches market size analysis [2022–2028] — global revenue, CAGR status, demanding regions, business strategies, SWOT analysis, industry revenue, growth opportunity — overall industry analysis and forecast report,” Sept. 23, 2022. [Online]. Available: <https://www.digitaljournal.com/pr/dip-switches-market-size-analysis-2022-2028-global-revenue-cagr-status-demanding-regions-business-strategies-swot-analysis-industry-revenue-growth-opportunity-overall-industry-analysis-and>
- [2] C. Weinold and C. S. Vista, “DIP switch with built-in active interfacing circuitry,” U.S. Patent 5,010,445, Apr. 1991. [Online]. Available: <https://www.freepatentsonline.com/5010445.html>
- [3] X. Lü *et al.*, “Automatic recognition of multiple weld types based on structured light vision sensor using deep transfer learning,” *IEEE Sens. J.*, vol. 23, no. 7, pp. 7142–7152, Apr. 2023.
- [4] D. W. Otter, J. R. Medina, and J. K. Kalita, “A survey of the usages of deep learning for natural language processing,” *IEEE Trans. Neural Netw. Learn. Syst.*, vol. 32, no. 2, pp. 604–624, Feb. 2021.
- [5] C. Wisultschew *et al.*, “Characterizing deep neural networks on edge computing systems for object classification in 3D point clouds,” *IEEE Sens. J.*, vol. 22, no. 17, pp. 17075–17089, Sept. 2022.
- [6] X. Zhao *et al.*, “Fusion of 3D LIDAR and camera data for object detection in autonomous vehicle applications,” *IEEE Sens. J.*, vol. 20, no. 9, pp. 4901–4913, May 2020.
- [7] S. Roy *et al.*, “Deep learning for classification and localization of COVID-19 markers in point-of-care lung ultrasound,” *IEEE Trans. Med. Imaging*, vol. 39, no. 8, pp. 2676–2687, Aug. 2020.
- [8] S. Hussein *et al.*, “Lung and pancreatic tumor characterization in the deep learning era: Novel supervised and unsupervised learning approaches,” *IEEE Trans. Med. Imaging*, vol. 38, no. 8, pp. 1777–1787, Aug. 2019.
- [9] F. Cristóvão *et al.*, “Investigating deep learning based breast cancer subtyping using pan-cancer and multi-omic data,” *IEEE/ACM Trans. Comput. Biol. Bioinf.*, vol. 19, no. 1, pp. 121–134, Jan. 2022.
- [10] J. Guo, W. Cao, B. Nie, and Q. Qin, “Unsupervised learning composite network to reduce training cost of deep learning model for colorectal cancer diagnosis,” *IEEE J. Transl. Eng. Health Med.*, vol. 11, pp. 54–59, Nov. 2022.
- [11] A. Jo and W. Lee, “Brass material analysis with deep-learning-based CdTe semiconductor x-ray fluorescence system,” *IEEE Trans. Nucl. Sci.*, vol. 69, no. 5, pp. 1085–1091, May 2022.
- [12] S. M. J. Jalali *et al.*, “New hybrid deep neural architectural search-based ensemble reinforcement learning strategy for wind power forecasting,” *IEEE Trans. Ind. Appl.*, vol. 58, no. 1, pp. 15–27, Jan. 2022.
- [13] E. Jeong *et al.*, “Deep learning inference parallelization on heterogeneous processors with TensorRT,” *IEEE Embed. Syst. Lett.*, vol. 14, no. 1, pp. 15–18, Mar. 2022.
- [14] K. Qiu, L. Tian, and P. Wang, “An effective framework of automated visual surface defect detection for metal parts,” *IEEE Sens. J.*, vol. 21, no. 18, pp. 20412–20420, Sept. 2021.
- [15] Y. Chen *et al.*, “Multi-source impact position identification method for metal plates based on fiber Bragg grating,” *IEEE Sens. J.*, vol. 22, no. 1, pp. 851–857, Jan. 2022.
- [16] A. Albanese, M. Nardello, G. Fiacco, and D. Brunelli, “Tiny machine learning for high accuracy product quality inspection,” *IEEE Sens. J.*, vol. 23, no. 2, pp. 1575–1583, Jan. 2023.
- [17] L. Xiao, B. Wu, and Y. Hu, “Surface defect detection using image pyramid,” *IEEE Sens. J.*, vol. 20, no. 13, pp. 7181–7188, July 2020.
- [18] Y. Zhang, D. Lefebvre, and Q. Li, “Automatic detection of defects in tire radiographic images,” *IEEE Trans. Autom. Sci. Eng.*, vol. 14, no. 3, pp. 1378–1386, July 2017.
- [19] S. Tian *et al.*, “CASDD: Automatic surface defect detection using a complementary adversarial network,” *IEEE Sens. J.*, vol. 22, no. 20, pp. 19583–19595, Oct. 2022.
- [20] Y. Peng *et al.*, “Automated product boundary defect detection based on image moment feature anomaly,” *IEEE Access*, vol. 7, pp. 52731–52742, Apr. 2019.
- [21] A. Dairi, F. Harrou, Y. Sun, and M. Senouci, “Obstacle detection for intelligent transportation systems using deep stacked autoencoder and k-nearest neighbor scheme,” *IEEE Sens. J.*, vol. 18, no. 12, pp. 5122–5132, June 2018.
- [22] A. Dairi, F. Harrou, M. Senouci, and Y. Sun, “Unsupervised obstacle detection in driving environments using deep-learning-based stereovision,” *Robot. Auton. Syst.*, vol. 100, pp. 287–301, Apr. 2018.
- [23] A. Setyanto, T. B. Sasongko, M. A. Fikri, and I. K. Kim, “Near-edge computing aware object detection: A review,” *IEEE Access*, vol. 12, pp. 2989–3011, Dec. 2023.
- [24] J. Gupta and S. Sharma, “Towards real time hardware based human and object detection: A review,” in *Proc. Int. Conf. Artif. Intell. Speech Technol. (AIST)*, 2022, pp. 1–6.
- [25] B. R. Solunke and S. R. Gengaje, “A review on traditional and deep learning based object detection methods,” in *Proc. Int. Conf. Emerg. Smart Comput. Inform. (ESCI)*, 2023, pp. 1–7.
- [26] Q. Ling and N. A. M. Isa, “Printed circuit board defect detection methods based on image processing, machine learning and deep learning: A survey,” *IEEE Access*, vol. 11, pp. 15921–15944, 2023.
- [27] J. Redmon and A. Farhadi, “YOLOv3: An incremental improvement,” *arXiv:1804.02767*, 2018.
- [28] A. Bochkovskiy, C.-Y. Wang, and H.-Y. M. Liao, “YOLOv4: Optimal speed and accuracy of object detection,” *arXiv:2004.10934*, 2020.
- [29] C.-Y. Wang, A. Bochkovskiy, and H.-Y. M. Liao, “YOLOv7: Trainable bag-of-freebies sets new state-of-the-art for real-time object detectors,” in *Proc. IEEE/CVF Conf. Comput. Vis. Pattern Recognit. (CVPR)*, 2023, pp. 7464–7475.
- [30] J. Glenn, “YOLOv5 release v7.0,” GitHub, 2021. [Online]. Available: <https://github.com/ultralytics/yolov5/releases/>
- [31] C. Li *et al.*, “YOLOv6 v3.0: A full-scale reloading,” *arXiv:2301.05586*, 2023.

- [32] D. Reis, J. Kupec, J. Hong, A. Daoudi, "Real-time flying object detection with YOLOv8," *arXiv:2305.09972*, 2023.
- [33] C.-Y. Wang, I.-H. Yeh, and H.-Y. M. Liao, "YOLOv9: Learning what you want to learn using programmable gradient information," *arXiv:2402.13616*, 2024.
- [34] K.-Y. Su, M.-F. Chen, P.-C. Tsai, and C.-H. Tsai, "Establish a dynamic detection system for metal bicycle frame defects based on YOLO object detection," in *Proc. IET Int. Conf. Eng. Technol. Appl. (IET-ICETA)*, 2022, pp. 1–2.
- [35] T. Ling, B. Zhang, Y. Zhang, and S. Yu, "Ship detection algorithm based on improved YOLOv5," in *Proc. IEEE Int. Conf. Automat. Control Robot. Eng. (CACRE)*, July 2021, pp. 483–487.
- [36] W. Yang and W. Zhang, "Real-time traffic signs detection based on YOLO network model," in *Proc. Int. Conf. Cyber-Enabled Distrib. Comput. Knowl. Discovery (CyberC)*, Oct. 2020, pp. 354–357.
- [37] S. Ikechukwu and E. Akin, "High performance network for detection of surface defects on hot-rolled steel strips based on an optimized YOLOv3," in *Proc. Int. Conf. Cyber-Enabled Distrib. Comput. Knowl. Discovery (CyberC)*, 2022, pp. 1–6.
- [38] W. Li, Z. Shen, and P. Li, "Crack detection of track plate based on YOLO," in *Proc. Int. Symp. Comput. Intell. Des. (ISCID)*, vol. 2, Dec. 2019, pp. 15–18.
- [39] C. Li, M. Shu, L. Du, H. Tan, and L. Wei, "Design of automatic recycling robot based on YOLO target detection," in *Proc. Asia Conf. Algorithms, Comput. Mach. Learn. (CACML)*, Mar. 2022, pp. 310–315.
- [40] M. Zhang and L. Yin, "Solar cell surface defect detection based on improved YOLO v5," *IEEE Access*, vol. 10, pp. 80804–80815, 2022.
- [41] H. Li *et al.*, "Enhanced YOLO v3 tiny network for real-time ship detection from visual image," *IEEE Access*, vol. 9, pp. 16692–16706, 2021.
- [42] L. Zhang *et al.*, "An automatic fault detection method of freight train images based on BD-YOLO," *IEEE Access*, vol. 10, pp. 39613–39626, 2022.
- [43] Y. Wang *et al.*, "PV-YOLO: Lightweight YOLO for photovoltaic panel fault detection," *IEEE Access*, vol. 11, pp. 10966–10976, 2023.
- [44] D. P. Carrasco, H. A. Rashwan, M. García, and D. Puig, "T-YOLO: Tiny vehicle detection based on YOLO and multi-scale convolutional neural networks," *IEEE Access*, vol. 11, pp. 22430–22440, 2021.
- [45] T.-H. Wu, T.-W. Wang, and Y.-Q. Liu, "Real-time vehicle and distance detection based on improved YOLO v5 network," in *Proc. World Symp. Artif. Intell. (WSAI)*, 2021, pp. 24–28.
- [46] Y. Ding *et al.*, "Long-distance vehicle dynamic detection and positioning based on GM-APD lidar and LIDAR-YOLO," *IEEE Sens. J.*, vol. 22, no. 17, pp. 17113–17125, 2023.
- [47] I. J. Goodfellow *et al.*, "Generative adversarial nets," *arXiv:1406.2661*, 2014.
- [48] T. Hinz, M. Fisher, O. Wang, and S. Wermter, "Improved techniques for training single-image GANs," in *Proc. IEEE Winter Conf. Appl. Comput. Vis. (WACV)*, Jan. 2021, pp. 1299–1308.
- [49] A. Radford, L. Metz, and S. Chintala, "Unsupervised representation learning with deep convolutional generative adversarial networks," *arXiv:1511.06434*, 2015.
- [50] M. Arjovsky, S. Chintala, and L. Bottou, "Wasserstein GAN," *arXiv:1701.07875*, 2017.
- [51] T. R. Shaham, T. Dekel, and T. Michaeli, "SiNGAN: Learning a generative model from a single natural image," in *Proc. IEEE/CVF Int. Conf. Comput. Vis. (ICCV)*, Oct. 2019, pp. 4569–4579.
- [52] I. Gulrajani, F. Ahmed, M. Arjovsky, V. Dumoulin, and A. Courville, "Improved training of Wasserstein GANs," in *Proc. Adv. Neural Inf. Process. Syst. (NeurIPS)*, Long Beach, CA, USA, Dec. 2017, pp. 5767–5777.
- [53] J. Redmon and A. Farhadi, "YOLO9000: Better, faster, stronger," in *Proc. IEEE Conf. Comput. Vis. Pattern Recognit. (CVPR)*, July 2017, pp. 6517–6525.
- [54] K. He, X. Zhang, S. Ren, and J. Sun, "Spatial pyramid pooling in deep convolutional networks for visual recognition," *IEEE Trans. Pattern Anal. Mach. Intell.*, vol. 37, no. 9, pp. 1904–1916, Sept. 2015.
- [55] S. Liu *et al.*, "Path aggregation network for instance segmentation," in *Proc. IEEE/CVF Conf. Comput. Vis. Pattern Recognit. (CVPR)*, June 2018, pp. 8759–8768.
- [56] C.-Y. Wang and H.-Y. M. Liao, "You only learn one Representation: Unified network for multiple tasks," *arXiv:2105.04206*, 2021.
- [57] X. Ding *et al.*, "RepVGG: Making VGG-style convnets great again," in *Proc. IEEE/CVF Conf. Comput. Vis. Pattern Recognit. (CVPR)*, June 2021, pp. 13728–13737.



Wei-Lung Mao was born in Taiwan, in 1972. He received his B.S. in electrical engineering from the National Taiwan University of Science and Technology (NTUST), Taipei, Taiwan, in 1994. He earned his M.S. and Ph.D. degrees in Electrical Engineering at the National Taiwan University (NTU), Taipei, Taiwan, in 1996 and 2004. He is now a Professor in the Department of Electrical Engineering and Graduate School of Engineering Science and Technology, National Yunlin University of Science and Technology (NYUST), Yunlin, Taiwan. His research interests are satellite navigation systems, intelligent and adaptive control systems, adaptive signal processing, neural networks, and precision control.

interests are satellite navigation systems, intelligent and adaptive control systems, adaptive signal processing, neural networks, and precision control.



Chun-Chi Wang was born in Taiwan in 1995 and received his B.A. from the Department of Materials and Energy Engineering, MingDao University, Changhua, Taiwan, in 2018. He earned his M.S. at the Graduate Institute of Aeronautical and Electronic Technology from National Formosa University (NFU), Yunlin, Taiwan, in 2021. He is currently a PhD student at the National Yunlin University of Science and Technology (NYUST), Yunlin, Taiwan. His research interests include automated image inspection, deep learning, robotic arm control systems, intelligent manufacturing production lines, and EtherCAT.



Po-Heng Chou (Member, IEEE) was born in Tainan, Taiwan. He received the B.S. degree in electronic engineering from National Formosa University (NFU), Huwei, Yunlin, Taiwan, in 2009, the M.S. degree in communications engineering from National Sun Yat-sen University (NSYSU), Kaohsiung, Taiwan, in 2011, and the Ph.D. degree from the Graduate Institute of Communication Engineering (GICE), National Taiwan University (NTU), Taipei, Taiwan, in 2020. His research interests include AI for communications, deep learning-based signal processing, wireless networks, and wireless communications, etc.

He was a Postdoctoral Fellow at the Research Center for Information Technology Innovation (CITI), Academia Sinica, Taipei, Taiwan, from Sept. 2020 to Sept. 2024. He was a Postdoctoral Fellow at the Department of Electronics and Electrical Engineering, National Yang Ming Chiao Tung University (NYCU), Hsinchu, Taiwan, from Oct. to Dec. 2024. He has been elected as the Distinguished Postdoctoral Scholar of CITI by Academia Sinica from Jan. 2022 to Dec. 2023. He is invited to visit Virginia Tech (VT) Research Center (D.C. area), Arlington, VA, USA, as a Visiting Fellow, from Aug. 2023 to Feb. 2024. He received the Partnership Program for the Connection to the Top Labs in the World (Dragon Gate Program) from the National Science and Technology Council (NSTC) of Taiwan to perform advanced research at VT Institute for Advanced Computing (D.C. area), Alexandria, VA, USA, from Jan. 2025 to present.

Additionally, Dr. Chou received the Outstanding University Youth Award and the Phi Tau Phi Honorary Membership from NTU in 2019 to honor his impressive academic achievement. He received the Ph.D. Scholarships from the Chung Hwa Rotary Educational Foundation from 2019 to 2020.



Yen-Ting Liu was born in Kaohsiung, Taiwan, in 2000. He received the B.S. degree in computer and communications engineering from the National Kaohsiung University of Science and Technology (NKUST), Kaohsiung, Taiwan, in 2022. He is currently studying for the M.S. degree in communications engineering from National Sun Yat-sen University (NSYSU), Kaohsiung, Taiwan. His research interests include deep learning in wireless communications, communication theory, and resource allocation for wireless networks.